

# Droplet transport in a nanochannel coated by hydrophobic semiflexible polymer brushes: the effect of chain stiffness

K. Speyer<sup>†</sup> and C. Pastorino<sup>\*,†</sup>

*\*Departamento de Física de la Materia Condensada, Centro Atómico Constituyentes, CNEA, Av.Gral. Paz 1499, 1650 Pcia. de Buenos Aires, Argentina, and <sup>†</sup> CONICET, Avenida Rivadavia 1917, C1033AAJ Buenos Aires, Argentina*

E-mail: pastor@cnea.gov.ar

## Abstract

We study the influence of chain stiffness on droplet flow in a nano-channel, coated with semiflexible hydrophobic polymers by means of non-equilibrium molecular-dynamics simulations. The studied system is then a moving droplet in the slit channel, coexisting with its vapor and subjected to periodic boundary conditions in the flow direction. The polymer chains, grafted by the terminal bead to the confining walls, are described by a coarse-grained model that accounts for chain connectivity, excluded volume interactions and local chain stiffness. The rheological, frictional and dynamical properties of the brush are explored over a wide range of persistence lengths. We find a rich behavior of polymer conformations and concomitant changes in the friction properties over the wide range of studied polymer stiffnesses. A rapid decrease in the droplet velocity was

---

\*To whom correspondence should be addressed

<sup>†</sup>\*Departamento de Física de la Materia Condensada, Centro Atómico Constituyentes, CNEA, Av.Gral. Paz 1499, 1650 Pcia. de Buenos Aires, Argentina

<sup>‡†</sup> CONICET, Avenida Rivadavia 1917, C1033AAJ Buenos Aires, Argentina

observed as the rigidity of the chains is increased for polymers whose persistence length is smaller than their contour length. We find a strong relation between the internal dynamics of the brush and the droplet transport properties, which could be used to tailor flow properties by surface functionalization. The monomers of the brush layer, under the droplet, present a collective “treadmill belt” like dynamics which can only be present due to the existence of grafted chains. We describe its changes in spatial extension upon variations of polymer stiffness, with bidimensional velocity and density profiles. The deformation of the polymer brushes due to the presence of the droplet is analyzed in detail. Lastly, The droplet-gas interaction is studied by varying the liquid to gas ratio, observing a 16% speed increase for droplets that flow close to each other, compared to a train of droplets that present a large gap between consecutive droplets.

## 1 Introduction

Different forms of liquid flow under high confinement regime has gained attention in the last years due to the importance in a broad range of areas, like biology<sup>1-3</sup>, medicine<sup>4</sup> and biotechnology<sup>5</sup>. Microfluidics deals with flows in the pico-liter scale, focusing on accurate manipulation of liquids and gases in micro and nano-channels. Lab-on-chip devices, where complex biochemical reactions are automated, are an example of promising applications in this field. Although large-scale industrial implementations are not available yet<sup>6</sup>, microfluidic devices are widely used in research laboratories<sup>4,5,7</sup>.

A low Reynolds number ( $Re$ ) and a high surface-area-to-volume ratio are characteristics of micro and nano-fluidics. Under these conditions, the flow is largely influenced by the confining substrate, which determines the boundary conditions. The no-slip boundary condition, usually assumed in macro scale calculations, is an approximation that is no longer valid in the micro-scale<sup>8</sup>. Efforts are being made to understand and control liquids in the picoliter scale, by changing the properties of the inner coating surfaces and modifying the interaction with the confined fluid. There are several factors that affect the slip, including wettability,

roughness, pressure, temperature or presence of undissolved gas and nanobubbles<sup>9</sup>. Several studies suggest that surface roughness influences greatly the boundary conditions of the flow<sup>9-13</sup>. A hierarchical structuration has been reported to reduce notably the friction<sup>14-16</sup>. There is consensus that hydrophobic coatings reduce friction, due to a weaker solid-fluid interaction<sup>17,18</sup>, but the underlying mechanism remains unclear<sup>19</sup>.

Droplet transport in micro and nanochannels have been thoroughly investigated in the last decade both theoretically<sup>10,20-22</sup> and experimentally<sup>23-27</sup>. Multi-phase flows are important for chemical and biotechnological applications, because they allow complex phenomena like chemical reactions, emulsions and interfaces<sup>28,29</sup> with the potential of tailoring technological applications. Cao et al<sup>10</sup> studied, by Molecular Dynamics (MD) simulations, the flow of a droplet in coexistence with its gas in a rough nanochannel. They observed that the slip can be largely influenced by the nano structuration of the hydrophobic walls. Slug flows are also present in polymer electrolyte membranes of fuel cells<sup>20,30-32</sup>, where water has to be eliminated from microchannels at a controlled rate, to maximize the efficiency of the device. In this context, Fukushima et al<sup>20</sup> studied the friction between a droplet and the confining walls of a microchannel, and its dependence on the channel width. A review on droplet based microfluidics can be found in Ref<sup>33</sup>.

Polymers tethered to a surface through a terminal monomer (polymer brushes) are good candidates to be used as coating in microchannels, due to their responsiveness to stimuli (pH, temperature, electric field, etc) and the ability to modify the rheological conditions<sup>34-39</sup>. Polymer brushes present a very wide range of applications, like pH-controlled nanopores<sup>40</sup>, catalysis in microreactors<sup>41</sup> and cell adhesion and detachment control<sup>42</sup>. The property of reducing friction of polymer brushes has been reported theoretically<sup>43-46</sup> and experimentally<sup>47-49</sup>. To understand this phenomenon, the boundary conditions of liquids past fully flexible polymer brushes has been extensively investigated, and slip lengths of different orders of magnitude have been observed<sup>47,50-57</sup>. In reference<sup>58</sup>, T. Kreer provides a recent and detailed review about the lubrication properties of polymer brushes.

Despite the numerous investigations in the field, little attention has been given to semiflexible polymer brushes under shear flow. Semiflexible polymer chains are an adequate coarse-grained model of macromolecules, whenever the dimensions of the macromolecule do not significantly exceed its persistence length. Kim et al.<sup>59</sup> studied via mean field calculations and computer simulations the response of semiflexible brushes under shear flow, and found good agreement between both methods in the high rigidity regime. Deng et al.<sup>52</sup> performed simulations of flow in microchannels coated with semiflexible polymers, to study glycocalyx fibers for 5 different values of bending rigidity. Flows are compared keeping constant the channel width, and varying the stiffness of the fibers. Römer and Fedosov<sup>60</sup> extend the study by Kim et al.<sup>59</sup> for high grafting densities, but restricted to stiff polymers. On a recent study, Singh et al.<sup>61</sup> studied the tribological behavior of polymer-coated bilayers via MD simulations, and found that the friction coefficient for semiflexible polymer brushes was higher than for a fully flexible brush. The comparison of both types of brushes is made at equal effective width of the channel, but different grafting densities. In a previous work<sup>62</sup>, we performed a comprehensive study of a nanochannel coated with semiflexible hydrophobic polymers, filled with a simple liquid. We found that for low grafting densities  $\rho_g$ , the rigidity of the chains has a direct influence in the slip length of the flow. To the best of our knowledge there is no comprehensive study of semiflexible polymer brushes in shear flow, that analyzes the rheological and chain properties of the system, covering the whole range of chain stiffness, from fully flexible polymers to very stiff rod-like polymers.

In this work, we perform MD simulations of a liquid-gas two-phase flow in a slit-like nanochannel, coated by a semiflexible hydrophobic polymer brushes (see Figure 1). This can be thought as the flow of a train of droplets through a brush-coated planar nanochannel, taking into account the periodic boundary conditions. The dependence of the droplet's velocity is analyzed by changing the distance between consecutive droplets in the axial direction of the channel, and varying the rigidity of the polymer chains. We investigate the friction forces acting on the liquid droplet due to the presence of a gaseous environment and

due to the confining polymer brush, for a wide range of chains' persistence lengths. We also studied the deformation of the soft substrate and the conformational changes of the polymers due to the liquid droplet, and how the brush-liquid interaction varies with bending stiffness. Lastly, the dynamics of the polymer's free-end is analyzed individually and collectively. In section 2 we provide details of the out-of equilibrium simulation technique, system geometry, physical conditions and molecular coarse-grained description. In section 3 we present the simulation results, focusing on droplet dynamics and single-chain and brush properties in successive subsections. We finish our work with a final discussion and concluding remarks in section 4.

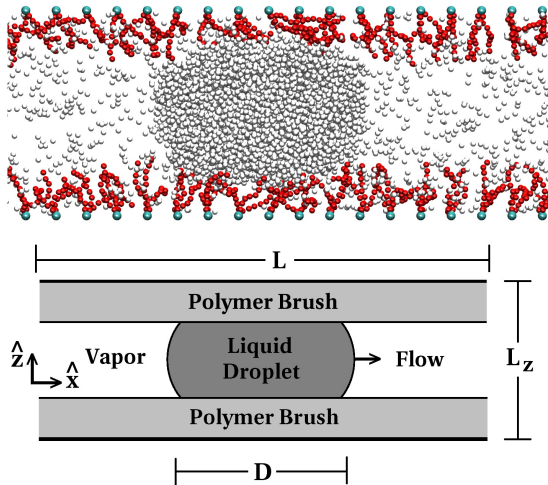


Figure 1: The system studied in this work consists of a slit like nano-channel, whose walls are separated by a distance  $L_z$ . Hydrophobic polymers anchored by a terminal bead to the walls coat the channel, generating a soft substrate. A liquid droplet in coexistence with its vapor fills the interior of the channel. A constant external force is applied to every particle to generate net flow of mass.  $D$  is the extent of the droplet in the direction of the flow ( $\hat{x}$ ) and  $L$  is the length of the simulation box in the same direction. Up: snapshot of the simulated system. Down: Schematic representation of the system.

## 2 Simulation Technique

Coarse-grained molecular dynamics (MD) simulations were performed at constant temperature, volume and number of particles. All particles interact with each other via a truncated

and shifted Lennard-Jones potential

$$U(r) = U_{LJ}(r) - U_{LJ}(r_c), r < r_c, \quad (1)$$

where  $r_c$  is the cut-off radius, and  $r$  is the distance between particles. Particle pairs whose distance exceeds the interaction cut-off, do not interact. The parameters of the Lennard-Jones potential depend on the pair of interacting particles

$$U_{LJ} = 4\varepsilon_{\alpha\beta}[(\frac{\sigma}{r})^{12} - (\frac{\sigma}{r})^6], \quad (2)$$

where the sub-indices  $\alpha$  and  $\beta$  stand for the different species. For monomer-monomer and fluid-fluid interactions  $\varepsilon$  takes the value of unity, and is the energy unit in the simulations. For fluid-monomer interactions the energy parameter was set to  $\varepsilon_{mf} = 1/3$ , which encodes the chemical affinity between the confining polymer brush and the liquid that flows through the channel. This value of  $\varepsilon_{mf}$  corresponds to a highly hydrophobic substrate, giving droplet contact angles around  $\theta_c \sim 145^\circ$ . The cut-off radius for this interactions was set to  $r_c = 2.24\sigma$ , which is twice the distance where the minimum of the potential is located. This election for the cut-off radius includes the attractive portion of the potential, allowing for the coexistence of a gaseous and a liquid phase. For monomer-monomer interactions, the cut-off radius was set to  $r_c = 1.12\sigma$ , to exclude attractive forces and simulate good solvent conditions. The particle diameter and mass were set to  $\sigma = 1$  and  $m = 1$  for all species, and these parameters are taken as the distance and mass units respectively. The time unit can be written in terms of these parameters as  $\tau = \sigma\sqrt{m/\varepsilon}$ .

The connectivity of the  $N = 10$  bead polymers chains is provided by the wide-spread Kremer-Grest model:

$$U_{FENE} = -\frac{1}{2}kR_0^2 \ln \left[ 1 - \left( \frac{r}{R_0} \right)^2 \right], r < R_0, \quad (3)$$

where the parameters were set to the usual values  $k = 30\varepsilon/\sigma^2$  and  $R_0 = 1.5\sigma$ . The finitely extensible nonlinear elastic (FENE) interaction is applied between consecutive monomers in a chain to account for the connectivity of each molecule.

To account for local stiffness of the polymer chains, a harmonic bending potential was implemented

$$U_{bend}(\theta) = 1/2k_b\theta^2, \quad (4)$$

where the angle  $\theta$  is defined between two consecutive segments along the molecule backbone. The orientation of consecutive segments and the angle  $\theta$  are related through the equation

$$\cos\theta = \frac{(\mathbf{r}_i - \mathbf{r}_{i-1}) \cdot (\mathbf{r}_{i+1} - \mathbf{r}_i)}{|\mathbf{r}_i - \mathbf{r}_{i-1}| |\mathbf{r}_{i+1} - \mathbf{r}_i|}, \quad (5)$$

where  $\mathbf{r}_i$  is the position of particle  $i$ .

The parameter  $k_b$  is the bending constant, which was varied in this work to modify the rigidity of the polymer brush. To quantify the rigidity of the chains, we introduce a dimensionless parameter  $l_p/l_c$ . The persistence length  $l_p$  is the distance over which segment orientation correlations are lost, and  $l_c$  is the contour length of the polymer. When the ratio of this magnitude is high ( $l_p/l_c \gg 1$ ), the polymer behaves like a rigid rod. On the other hand, a polymer with a low value of this quotient ( $l_p/l_c \ll 1$ ) behaves like a flexible chain. To estimate the persistence length of the polymers, we used the exponential decay of the orientational correlation of the bonds as in Ref<sup>63</sup>:

$$\langle \cos \theta_s \rangle = \exp[-s \cdot a/l_p], \quad (6)$$

where  $s$  is the distance in monomer units,  $a$  is the mean distance between beads. For consecutive segments ( $s = 1$ ), this equation yields

$$l_p = -a / \ln \langle \cos \theta_1 \rangle \quad (7)$$

The Velocity Verlet scheme was implemented to integrate the trajectories of the particles in the simulation, with time step  $\delta t = 3 \cdot 10^{-4}$ . Approximately  $6 \cdot 10^7$  steps were performed for each simulation, including  $\sim 10^6$  relaxation steps. To maintain a constant value of temperature during the simulations, the dissipative particle dynamics (DPD) algorithm was applied<sup>64-66</sup>. The equations of motion are modified as follows:

$$\mathbf{F} = \mathbf{F}_C + \mathbf{F}_R + \mathbf{F}_D, \quad (8)$$

where  $\mathbf{F}_C$  is the sum of the conservative forces,  $\mathbf{F}_R$  is a random force and  $\mathbf{F}_D$  is the dissipative force. All forces are applied in pairs, abiding Newton's third Law, therefore conserving momentum locally. For each interacting pair, a random force is calculated as follows:

$$\mathbf{F}_R = \zeta \omega_R(r) \eta \hat{\mathbf{r}}, \quad (9)$$

where  $r$  is the distance between particles,  $\hat{\mathbf{r}}$  is the unity vector joining a given pair of particles,  $\zeta$  is a parameter that modifies the strength of the force,  $\eta$  is a random number generated for each occurrence, and the weight  $\omega_R$  is a function of the distance between particles. The dissipative Force is:

$$\mathbf{F}_D = -\gamma \omega_D(r) (\hat{\mathbf{r}} \cdot \mathbf{v}) \hat{\mathbf{r}}, \quad (10)$$

where  $\gamma$  is the friction constant,  $\mathbf{v}$  is the difference of velocities of the particles, and  $\omega_D$  is also a weight function. The parameters and functions were chosen to fulfill the fluctuation-dissipation theorem, which happens for the relations:  $\zeta^2 = 2k_B T \gamma$  and  $\omega_R^2(r) = \omega_D(r)$ . The usual choice for these weight functions was made<sup>67</sup>, and the friction constant was set to  $\gamma = 0.5$ . All simulations were performed at a fixed temperature value  $T = 0.8\varepsilon/k_B$ . At this temperature, the Lennard-Jones fluid separates into two phases: a liquid phase of density  $\rho_l = 0.69\sigma^{-3}$ , and a vapor phase of density  $\rho_v = 0.03\sigma^{-3}$ .

Periodic boundary conditions were applied in the directions parallel to the walls ( $\hat{x}$  and  $\hat{y}$ ), while in the remaining direction ( $\hat{z}$ ) a purely repulsive and smooth 9-3 potential  $U_{wall}$  was implemented to prevent the particles from escaping the simulation box and to provide a planar channel geometry for the system.

$$U_{wall}(z) = A_w \left[ \left( \frac{\sigma}{z} \right)^9 + \left( \frac{\sigma}{z} \right)^6 \right], \quad (11)$$

with  $A_w = 3.2$ . The simulation box dimensions are  $L_x \times L_y = 13.42\sigma \times L_z$ , where the length of the simulation box in the flow direction was varied between  $35\sigma < L_x < 900\sigma$ , and wall to wall distances were adjusted in the range  $30\sigma < L_z < 40\sigma$ .

The polymer brush is composed of linear polymer chains of  $N = 10$  beads each, with a terminal monomer fixed to a wall. The grafting density (number of chains per unit area) was set to  $\rho_g = 0.05\sigma^{-2}$  for all simulations, and the grafted sites were arranged in an ordered square lattice of parameter  $a_l = 1/\sqrt{\rho_g} = 4.47\sigma$ . A uniform distribution of grafting sites was chosen to avoid large inhomogeneities in the polymer density profile that can appear in small system with low  $\rho_g$  when the chain heads are randomly scattered. We think that this way of distributing the chains is more representative than the random like, because the latter can produce singular physical phenomena that depend on the particular arrangement of the polymers, specially for the relatively small samples used in the simulations.

To favor a perpendicular orientation of the polymers with respect to the channel walls, a virtual bead is added to each polymer chain in the bending force calculation. This virtual bead is placed below the grafted monomer, and when the bending force is calculated, the bond between this bead and the grafted end-bead is used to calculate a bending force on the second bead of the chain. This force tends to align the first mobile monomers of the chain in the direction perpendicular to the wall, and to induce a stretching of the polymers towards the center of the channel.

An external force is applied to all particles in the system during the simulations to create

a flow, and take the system out of equilibrium. This body force is constant and is applied in a direction parallel to the walls of the channel ( $\hat{x}$ ). The value  $f_{ext} = 0.002\varepsilon/\sigma$  was chosen to obtain particle velocities in the range  $0.1\sigma/\tau < v < 0.5\sigma/\tau$  which are high enough to extract significant data in a reasonable computation time, and is low enough to be in a near-equilibrium regime.

## 3 Results

### 3.1 Liquid - Polymer Brush Interface

In this section we analyze the interaction between semiflexible polymers grafted to the interior walls of the nanochannel and a liquid drop flowing through it. The polymer-liquid interaction potential parameters were chosen such that the droplet is in super-hydrophobic regime (Casie-Baxter state). We focus our attention on the influence of the polymer rigidity on the droplet flow, which is studied by varying the bending constant  $k_b$  (see Eq. 4) in the range  $0 \leq k_b \leq 160\varepsilon$  or, in terms of persistence length over contour length, in the range  $0.1 \leq l_p/l_c \leq 20$ . The length of the channel in the  $\hat{x}$  direction was set to  $L = 107\sigma$  for this set of simulations, while the extension of the droplet in the same direction is approximately  $D = 30\sigma$ . The droplet trajectory is tracked, and the mean velocity is calculated performing a linear fit. Details of the non-trivial tracking algorithm for the center of mass of the droplet are presented in the Supporting Information. It is not straight forward to compare systems with different degrees of local stiffness, because the polymer extension depends strongly on  $k_b$ . A hard bending potential will give rise to a polymer brush of larger height, consequently decreasing the effective width of the channel and compressing the droplet. We kept constant the effective channel width in order to isolate the influence of bending rigidity on the flow, by comparing the shape of the droplets inside the channels. To maintain the shape of the droplet similar for all the studied bending rigidities, it is necessary to adjust the distance between walls ( $L_z$ ). The case of totally flexible chains ( $k_b = 0$ ) was taken as reference

to compare the two-dimensional density profiles of the droplets. For each system (i.e. for each value of bending constant  $k_b$ ), various simulations were performed for different channel widths ( $L_z$ ), to find the droplet shape that most resembles the reference case. Details of this procedure are provided in the Supporting Information.

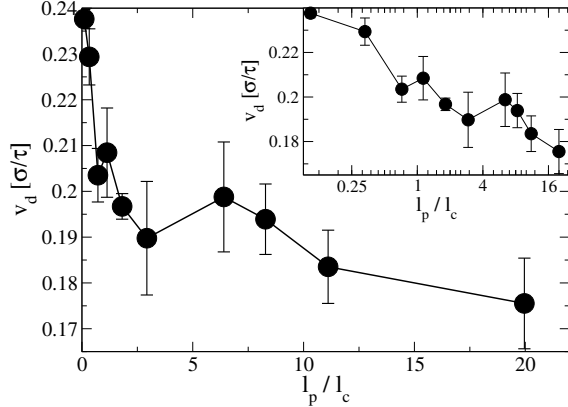


Figure 2: Droplet velocity versus persistence length of the polymers. Two different regimes can be observed: for persistence length smaller than the contour length, the velocity diminishes rapidly. For persistence lengths greater than the contour length, the droplet’s velocity decreases with persistence length, but at a much more slower rate. The inset shows the droplet velocity plotted against the persistence length in a semi-log graph to highlight the behavior at low persistence lengths.

In Figure 2 the droplet velocity is plotted against bending rigidity. The large error bars are due to the uncertainty to determine the channel width ( $L_z$ ), to obtain similar droplets for all bending rigidities. To quantify the rigidity of the polymers, we utilized the dimensionless parameter  $l_p/l_c$ , where  $l_p$  is the persistence length and  $l_c$  is the contour length, as explained in section 2. For persistence lengths ( $l_p$ ) smaller than the contour length ( $l_c$ ), the velocity of the droplet decays rapidly with increasing stiffness, while for  $l_p/l_c > 1$  the velocity of the droplet decreases slowly with rigidity. The general tendency is that increasing the rigidity of the polymer, reduces the droplet velocity.

To gain insight into the friction dependence on chain stiffness, the average of the product of the density profiles between liquid and brush is plotted against rigidity in Figure 3. This quantity is proportional to the number of brush-liquid interactions<sup>68</sup>. It is interesting to observe the non-monotonic dependence of the number of monomer-droplet particle interactions

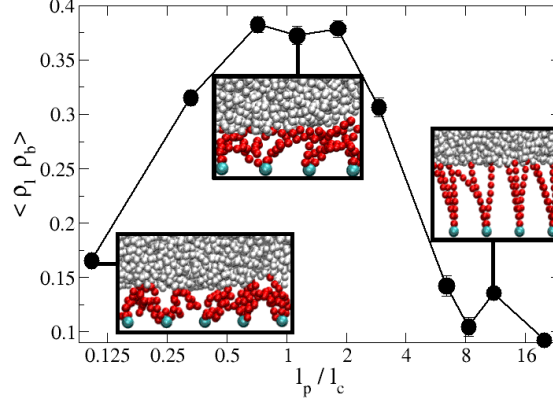


Figure 3: Average of the product of liquid and brush densities. It is proportional to the number of interactions between brush and droplet. Insets: morphology of the brush polymer layer for fully flexible polymers,  $l_p/l_c = 0.1$  (left) medium stiffness,  $l_p/l_c = 1.1$  (center) and very high stiffness,  $l_p/l_c = 11$  (right). The vapor particles are not shown in order to have a clear visualization of the polymer chains.

with the polymer rigidity (see Figure 3). As shown in the left inset of Figure 3, the fully flexible chains ( $l_p/l_c \ll 1$ ) are in a mushroom regime. The polymers wrap themselves to maximize conformational entropy and do not penetrate the liquid phase so frequently. More rigid polymers ( $l_p/l_c \simeq 1$ ) adopt a banana-like shape, due to the drag force exerted by the liquid droplet. This exposes more beads of each chain to the droplet, thus increasing the number of brush-liquid interactions. On the other hand, highly rigid polymers ( $l_p/l_c \gg 1$ ) tend to extend themselves in the direction perpendicular to the substrate. The low inclination angle of these stiff polymers hinders the non-terminal beads from reaching the liquid phase. Only the free end-bead monomers of each chain are in contact with the droplet, thus reducing the number of collisions. It is important to note that the hydrophobicity between liquid and polymers warrants a Cassie-Baxter regime in all cases, but with a significantly different structure of the polymer brush. The number of monomer-liquid interactions alone cannot account for the dependence of the droplet velocity on bending rigidity, observed in Fig. 2. This implies that there is another property of the system that varies with  $l_p$  and explains the decrease in the flow.

The 2-dimensional terminal-bead distribution density (see Figure 4) shows how the brush

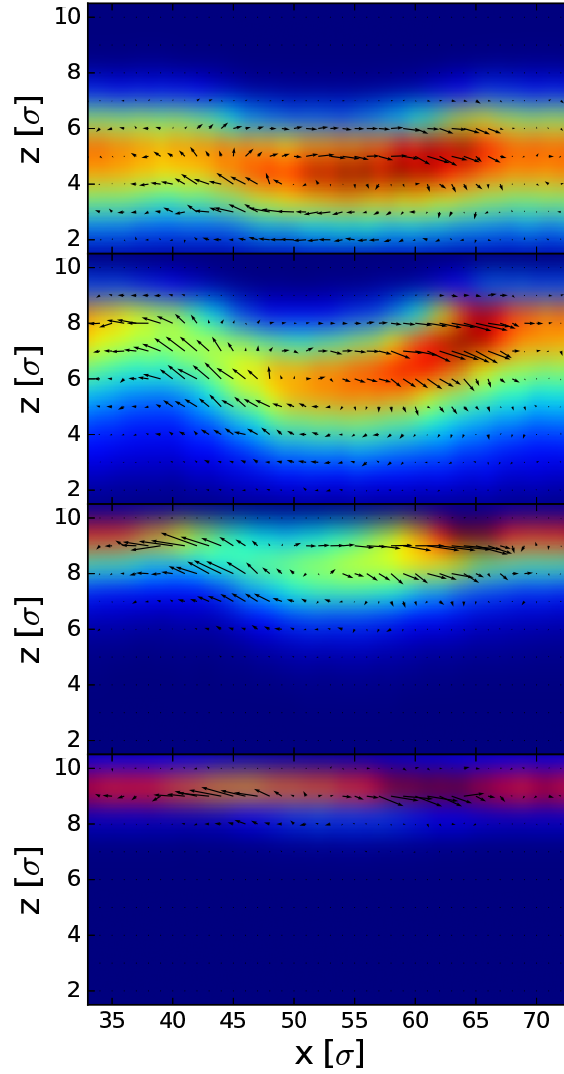


Figure 4: The polymer's end-bead distribution is shown as a color map. Green and yellow zones represent high presence of terminal monomers, while blue zones represent low density of terminal beads. The red arrows, composing a vector field, represent the mean momentum of the end-beads of the polymers. These graphs are presented for various rigidities, from top to bottom:  $l_p/l_c = 0.1; 0.72; 2.9; 8.3$ .

is deformed by the liquid droplet, for different values of bending rigidity. In every case the brush near the advancing end of the droplet (right) is denser than near the back (left). This is due to the liquid particles colliding with the polymers, pushing them forward, squeezing the monomers near the advancing end of the droplet. It is also observed that the brush composed of slightly rigid chains ( $l_p/l_c = 0.33$ ) suffers a stronger deformation by the droplet, than the brush composed of fully flexible polymers ( $l_p/l_c = 0.1$ ). The latter is denser, hence there are more excluded volume interactions impeding the compression of the brush. For very rigid chains ( $l_p/l_c \geq 6.4$ ), the end-bead distribution narrows, and its mean value gets closer to the center of the channel, due to the polymer elongation in  $\hat{z}$ .

To analyze the collective motion of the brush, the terminal-beads momentum vector field is plotted over the density profile (black arrows in Figure 4). From this graph it is possible to extract qualitative information about the dynamics of the polymer brush. First, it can be noted that for all degrees of stiffness, the polymers that are in contact with the advancing end of the droplet (right side in Fig. 4), tend to have a velocity in the direction of the flow and towards the wall. The droplet collides with the polymers in the flow direction, and compresses the brush towards the channel walls. Second, near the receding contact angle of the droplet (left region of the graphs in Fig. 4), the brush has a mean velocity towards the center of the channel, in the  $\hat{z}$  direction. The liquid applies a force on the brush perpendicularly to the grafting plane ( $\hat{z}$ ), pressing the end bead of the chains near the wall. When the droplet passes, the force on the chains is no longer applied, and the free ends rise towards the center of the channel.

In third place, for flexible polymers, the layer in contact with the liquid droplet has a positive mean velocity, while the terminal monomers near the wall have a mean velocity in the direction opposite to the flow. This collective dynamics resembles the motion of a treadmill belt. A similar behavior has been reported for flexible polymer brushes under shear: a velocity profile which is negative in the interior of the brush layer, and positive near the brush-liquid interface<sup>69,70</sup>. This velocity profile is the result of individual polymers

performing a cyclic motion, which consist of polymers stretching in the direction of the flow after spontaneous excursions inside the liquid driven by thermal fluctuations. Afterwards the chains retracts to the grafted site closer to the wall, to maximize their configurational entropy. The bending potential hinders the cyclic motion of the polymer chains, because it competes with the configurational entropy, stretching the chains and inhibiting the retraction movement<sup>62</sup>. Increasing the persistence length of the polymers, flattens the velocity profile of the polymer brush.

To exhibit the influence of the brush dynamics on the flow observed in Figure 4, we examined the velocity of the brush in contact with the liquid. As mentioned before, the region of space where brush and droplet interact will be given by the overlap of the liquid density  $\rho_l(\mathbf{r})$  and brush density  $\rho_b(\mathbf{r})$ . Zones of high brush-droplet interaction are portrayed by a high value of the product of the liquid and brush densities  $\rho_l(\mathbf{r})\cdot\rho_b(\mathbf{r})$ , while a null value of  $\rho_l(\mathbf{r})\cdot\rho_b(\mathbf{r})$  indicates vanishing brush-liquid interaction. We define the brush boundary layer velocity as:

$$v_b^{(BL)} \equiv \frac{\int d\mathbf{r} \rho_l(\mathbf{r}) \rho_b(\mathbf{r}) v_b(\mathbf{r})}{\int d\mathbf{r} \rho_l(\mathbf{r}) \rho_b(\mathbf{r})}, \quad (12)$$

where  $v_b(\mathbf{r})$  is the velocity field of the monomers composing the polymer brush,  $\rho_b(\mathbf{r})$  and  $\rho_l(\mathbf{r})$  are the brush and liquid number densities, respectively. This magnitude ( $v_b^{(BL)}$ ) is the weighted average brush velocity, where the weight is given by the product of the brush and liquid densities. To take into account only the liquid phase, and leave the vapor contribution out, we set the liquid density to  $\rho_l(\mathbf{r}) = 0$ , if the fluid density is below the average of the equilibrium liquid and gas densities. Analogously we define the liquid boundary layer velocity as:

$$v_l^{(BL)} \equiv \frac{\int d\mathbf{r} \rho_l(\mathbf{r}) \rho_b(\mathbf{r}) v_l(\mathbf{r})}{\int d\mathbf{r} \rho_l(\mathbf{r}) \rho_b(\mathbf{r})}, \quad (13)$$

which can be interpreted as the mean velocity of the liquid in contact with the polymer brush.  $v_l(\mathbf{r})$  is the velocity field of the liquid phase.

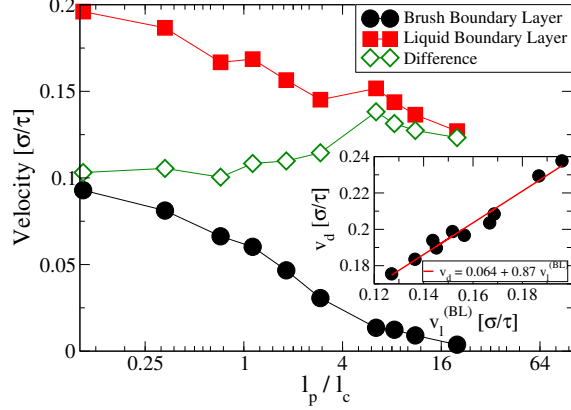


Figure 5: Velocity of the brush (black circles) and liquid (red squares) in the brush-liquid interface are plotted as a function of persistence length. The difference between these velocities, shows how the liquid boundary layer passes over the brush boundary layer (open green diamonds). Inset: droplet velocity versus the liquid boundary layer velocity. The liquid boundary layer velocity is closely related to the effective slip boundary condition for the flow.

The brush boundary layer velocity ( $v_b^{(BL)}$ ) and the liquid boundary layer ( $v_l^{(BL)}$ ) velocity are plotted against persistence length in Figure 5.  $v_l^{(BL)}$  is closely related to the effective slip boundary condition of the flow of the simple liquid inside the channel, used in hydrodynamic calculations. Assuming a poiseuille flow near the center of the liquid phase, the droplet velocity should depend linearly on the slip velocity  $v_s$ , with a slope equal to one. In the inset of Figure 5, the droplet velocity ( $v_d$ ) is plotted against  $v_l^{(BL)}$ . It can be observed that  $v_d$  varies linearly with the liquid boundary layer velocity  $v_l^{(BL)}$ , with a slope of 0.87. Therefore, we can roughly identify  $v_l^{(BL)}$  as the effective slip boundary condition imposed by the polymer brush on the droplet flow.

It is interesting to analyze the brush boundary layer velocity  $v_b^{(BL)}$  as rigidity increases (see black circles in Figure 5). For flexible polymers ( $l_p/l_c \ll 1$ ),  $v_b^{(BL)}$  has the same order of magnitude as the droplet velocity, while for stiff chains ( $l_p/l_c \gg 1$ ),  $v_b^{(BL)}$  drops to zero. The overall average brush velocity is null, because the chains are grafted to the static walls. The dynamics of the flexible polymers in the brush reduces the friction between liquid and substrate, by adopting a positive velocity near the liquid and a negative velocity near the wall (see Figure 4). As chain stiffness increases, the cyclic motion of the polymers is hindered,

because the bending rigidity impedes the wrap and recoil movement<sup>62</sup>. This “treadmill belt” like dynamical behavior of the chains affects heavily the final velocity of the droplet. The correlation coefficient between the droplet velocity and the brush boundary layer velocity is  $corr(v_d, v_b^{(BL)}) = 0.91$ . To the best of our knowledge, there is no previous quantitative work that shows that the internal dynamics of a polymer brush can affect the droplet flow.

We also define the  $\delta v$  as the difference between the liquid boundary layer velocity  $v_l^{(BL)}$  and the brush boundary layer velocity  $v_b^{(BL)}$ . This magnitude measures how the liquid boundary layer passes the brush boundary layer.  $\delta v$  maintains a fairly constant value in the range  $l_p/l_c < 4$ , and for  $l_p/l_c > 4$  there is a sudden increase. This change in the behavior of  $\delta v$  coincides with the decrease of the number of polymer-liquid interactions (see Figure 3). We think that the liquid boundary layer velocity relative to the brush boundary layer increases with rigidity, due to the decrease of polymer-liquid interactions.

To summarize the effect of polymer’s bending rigidity on flow properties, we can distinguish two factors. First, the internal dynamics of the polymers facilitates the liquid flow for flexible polymers. This effect is hindered as the chain’s bending rigidity increases. Secondly, the way in which the closest layers of liquid and brush slide past each other. The sliding of liquid relative to the brush is enhanced for large persistence lengths ( $l_p/l_c > 1$ ). These two effects compete with each other, and the overall brush motion seems to have a more determinant role on the droplet’s velocity.

### 3.2 Brush and chain properties

In the previous section we have shown that the dynamics of the polymer chains affects the rheological properties inside the nano-channel. The influence of brush deformations on friction forces has also been reported in a recent study<sup>71</sup>. Therefore, it is worth studying the conformation and dynamical behavior of the polymer brush.

To quantify the deformation of the brush in the flow direction ( $\hat{x}$ ), the  $\hat{x}$  component of the end-to-end vector ( $\mathbf{R}$ ) is plotted against the  $x$  coordinate for various degrees of rigidity

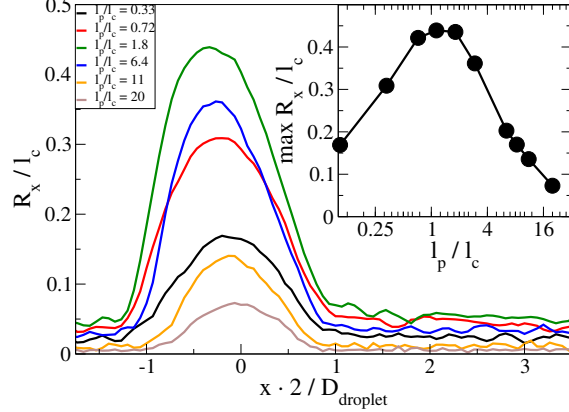


Figure 6: End-to-end brush vector component in the flow direction ( $\hat{x}$ ) versus position ( $x$ ), normalized by the droplet size ( $D$ ). Data is analyzed in the droplet frame of reference, where the center of mass of the droplet is always on  $x = 0$ . Inset: Maximum inclination of the end-to-end brush vector component in the direction of the flow ( $\hat{x}$ ) versus rigidity ( $l_p/l_c$ ). A non-monotonic behavior can be observed as the rigidity of the polymers increases (see text).

in Figure 6. It can be observed that near the center of mass of the droplet ( $x = 0$ ), the inclination of the chains reaches a maximum in all cases. This is due to droplet passing over the polymer brush, elongating the chains in the direction of the flow. The graph shows that the chain inclination profiles depend on the rigidity in a non-monotonic way. To expose this dependence, the maximum inclination is plotted versus the persistence length of the chain (see Inset of Figure 6). Flexible chains ( $l_p/l_c < 1$ ) tend to wrap themselves, to maximize their configurational entropy. Increasing the bending rigidity induces a coherent stretching along the chain, increasing the distance between the terminal monomers of the chains. When the persistence length ( $l_p$ ) is similar to the contour length ( $l_c$ ) the displacement of the chains reaches a maximum ( $l_p/l_c \simeq 1$ ), and for  $l_p/l_c > 1$  it decreases. The first bond of the polymer chains is oriented perpendicular to the wall (see section 2), which favors a vertical direction of elongation. For  $l_p/l_c \gg 1$  the angles between consecutive bonds are strongly correlated through the whole chain, thus the orientation of the first bond (in  $\hat{z}$ ) endures until the last monomer. In this regime, bending forces hinder the bonds to reach large angles between consecutive monomers, therefore the elongation of the chains takes place mainly in the direction perpendicular to the wall and not in the parallel direction.

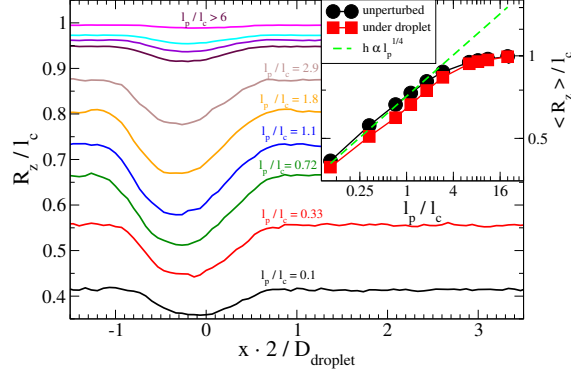


Figure 7: Profile of the end-to-end brush vector component in the direction perpendicular to the walls ( $\hat{z}$ ) versus  $x$  coordinate, in the droplet frame of reference. The horizontal axis is normalized, dividing by the length of the droplet in the direction of the droplet velocity. Inset: Mean value of  $R_z$  unperturbed (black circles) and under the droplet (red squares) in a log-log plot. The dashed line is the scaling law predicted by Mean Field theory<sup>72</sup>.

In Figure 7, the profile of the vertical component of the end-to-end vector ( $R_z$ ) is presented for every studied bending rigidity. The height of the brush increases monotonically with the bending rigidity, and in all cases the profile of  $R_z$  presents a minimum near the droplet's center of mass. The droplet applies pressure on the polymer brush, decreasing its height locally. To have a better visualization of the behavior of the polymers, the mean height of the polymers in the presence of the droplet  $|x| < D_{\text{droplet}}$  and far away from it  $|x| > D_{\text{droplet}}$  are plotted against rigidity, in the inset of Figure 7. The height of the brush, unaffected by the droplet, scales as  $h \propto l_p^{1/4}$  with persistence length (dashed line), and for  $l_p/l_c \gg 1$  the increase rate diminishes due to finite extension effects. The scaling law of brush height with persistence length was first proposed by Birshtein and Zhulina<sup>72</sup> for semiflexible polymer brushes in mushroom regime (see Table I). A similar behavior for the unperturbed brush height was also observed by Kim et al.<sup>59</sup>, who performed Lattice-Boltzmann and Brownian-Dynamics simulations (see their Figure 3b), and by Milchev and Binder<sup>73</sup> by MD simulations (see their Figure 2b). The vertical extension of the polymers under the droplet (red squares) follows basically the same behavior, but with small deviations. These are due to the different compressibilities of the brush, which vary with the bending rigidity.

To quantify the perturbation of the brush due to the presence of the liquid, in Figure 7,

we calculated the mean value of the unperturbed brush height minus the minimum of the  $R_z(x)$  profile. This is plotted as a function of bending rigidity in Fig. 8 (black circles). The deformation of the brush, caused by the presence of the droplet, is maximum for persistence lengths similar to the contour lengths ( $l_p/l_c \simeq 1$ ). Fully flexible polymer-brushes ( $l_p/l_c \ll 1$ ) are more dense than brushes composed of semi-flexible chains, and the excluded volume interactions between monomers hinders the compression of the brush. In the other extreme, very rigid polymers ( $l_p/l_c \gg 1$ ) are also difficult to compress vertically, because chains are strongly stretched in the direction perpendicular to the wall, to reduce the elastic energy. A compression towards the wall requires a high energy to compensate the increase in elastic energy. In between these regimes ( $l_p/l_c \simeq 1$ ), the brush deformation reaches a maximum. In this case the segments in each chain elongate coherently in a defined direction, and the polymers adopt a banana-shape configuration, when compressed by the droplet. This particular conformation allows for an easier compression than the fully flexible chains, because in this range ( $l_p/l_c \simeq 1$ ), the bending potential is softer than the excluded volume potential.

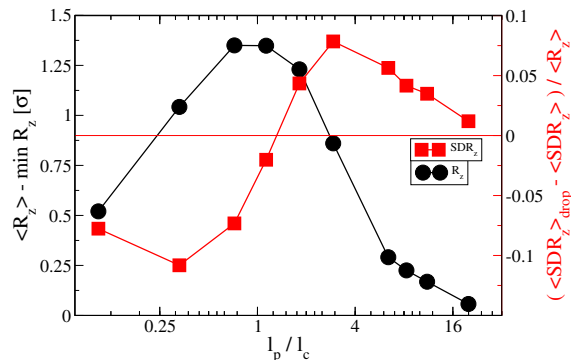


Figure 8: Difference between vertical stretching of the polymers under the droplet and far away from it (black circles). This magnitude quantifies the deformations of the brush in the directions perpendicular to the wall, due to the presence of the droplet. In red squares, it is shown the mean displacement of the end-to-end vector under the droplet with respect to the unperturbed displacement in the direction perpendicular to the wall. This magnitude gives an idea of the typical movement of the polymer’s end-bead, and how it changes in the presence of the droplet. For low rigidities the displacement is hindered, while for high rigidities the end-bead movement is enhanced.

The dynamics of the polymer chains change qualitatively with the bending constant  $k_b$ .

The standard deviation of the end-to-end vector distribution quantifies the movement of the free end of each chain with respect to its mean position. By calculating the standard deviation of  $R_z$  for polymers under the droplet and far away from it, it is possible to shed light on the influence of the liquid in the dynamics of the chains. In Figure 8 the difference between the mobility of the terminal bead in the presence of the liquid and far away from the droplet is plotted against stiffness (red squares). A negative value means that the presence of the droplet hinders the motion of the chains, while a positive value means that the interaction droplet-brush enhances chain mobility. For flexible polymers, the space that the terminal bead can explore is limited by the contour length of the polymer, due to the connectivity of the molecule. In the presence of a droplet, the available space to explore is reduced, as the chain does not penetrate significantly in the liquid phase. This leads to a reduction in the mobility of the polymers. Stiffer polymers extend in the direction perpendicular to the wall ( $\hat{z}$ ), and in the presence of a liquid droplet they bend, forming an arc. For  $l_p/l_c > 1.4$ , the bending potential is hard enough such that the curved chains elongate frequently in  $\hat{z}$ , and penetrate in the droplet. This leads to an increase in the chain mobility in the direction perpendicular to the wall.

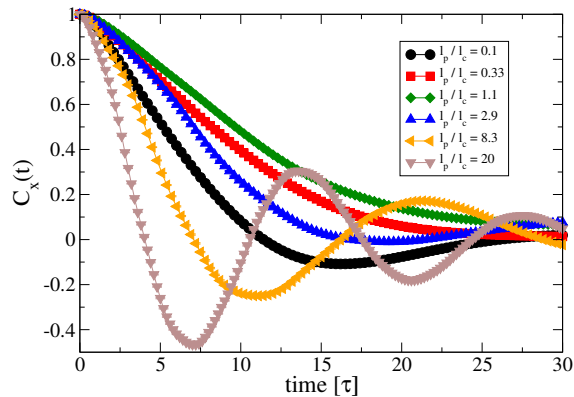


Figure 9: Time autocorrelation function of the  $\hat{x}$  component of the end to end vector for different values of rigidity. The values of relative stiffness  $l_p/l_c$  are shown in the legend.

To gain further insight in the mean individual polymer dynamics, the time autocorrelation function of the end-to-end vector in the direction of the flow was calculated for several values

of stiffness (see Figure 9). This quantity is defined as

$$C_x(t) = \frac{\langle R_x(0) \cdot R_x(t) \rangle - \langle R_x^2 \rangle}{\langle R_x \rangle^2 - \langle R_x^2 \rangle}, \quad (14)$$

where  $\langle f \rangle$  denotes the time average of  $f$ . The effect of the bending forces is evidenced in the oscillatory motion of the stiffest chains  $l_p/l_c \gg 1$ . As expected, the more rigid the bending potential, the higher the oscillation frequency. For  $l_p/l_c < 3$  no oscillatory motion can be observed. A decay of  $C_x(t) \rightarrow 0$  can be observed in all cases, which corresponds to the decorrelation of the trajectory of the free end of the polymers.

### 3.3 Fluid Dynamics

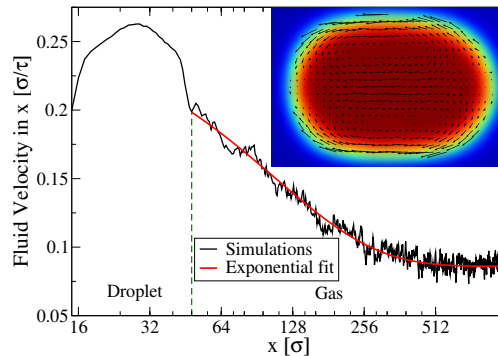


Figure 10: Fluid velocity in the direction of the flow ( $\hat{x}$ ) as a function of the  $x$  coordinate (in log scale). The droplet ( $x < 48\sigma$ ) travels at a higher velocity than the vapor phase ( $x > 48\sigma$ ). It is also possible to observe that gas velocity decays exponentially with  $x$ . Fitting the fluid velocity by an exponential function, a relaxation length ( $l_{rel}$ ) was obtained for the gas  $l_{rel} = 107\sigma$ . The terminal velocity of the gas  $v_\infty$  (far away from the droplet) coincides with the simulations done in the absence of a liquid phase. Inset: 2-dimensional density profile of the droplet, with the liquid velocity field overlaid. The velocities are calculated in the frame of reference of the center of mass of the droplet.

In this section we study the properties of the two-phase liquid and gas flows in the nanochannel. The fluid velocity at  $z = L_z/2$  is plotted as a function of the  $x$  coordinate in Figure 10 for a long channel ( $L = 900\sigma$ ). The droplet, located in  $x < 48\sigma$ , has a higher

velocity than the gas ( $x > 48\sigma$ ). The velocity of the gas near the droplet matches the velocity of the liquid, and then decays exponentially to the terminal velocity  $v_\infty = 0.85\sigma/\tau$ . By fitting the velocity profile of the gas with an exponential function, the characteristic relaxation length of the gas was found to be  $l_{rel} = 107\sigma$ .

The internal velocity field of the droplet is shown in the inset of Figure 10. A recirculation flow is observed with two stagnation points near the brush-liquid interface. Similar vector fields were reported by Günther et al.<sup>23</sup> for experiments on liquid segments in microchannels, in coexistence with gas (see their Figure 5b). This internal flow affects the droplet velocity, due to the viscous dissipation.

The difference between the gas and liquid velocities implies that the droplet moves relative to the surrounding gas. Therefore, the liquid suffers a drag force applied by the coexisting vapor. If the channel is not long enough to allow for the gas phase to relax ( $L \leq 2l_{rel}$ ) and adopt its terminal velocity, then the mean gas velocity will be closer to the velocity of the droplet. Because the gas friction force is proportional to the velocity difference between vapor and droplet, in a short channel the friction will be lower, thus producing a faster moving droplet, as seen in Figure 11. This can be also observed by noting that due to the periodic boundary conditions in  $\hat{x}$ , the channel length  $L$  is equal to the distance between consecutive droplets in an infinitely long channel. The system represents a train of droplets, each at a fixed distance, given by  $L$ . If the distance between adjacent droplets is large, then the gas between them relaxes and adopts the terminal gas velocity  $v_\infty$ . This will enhance the velocity difference between gas and droplet, which is proportional to the friction force, thus slowing the droplets down.

To portray the gas-liquid interaction, a set of simulations were performed only varying the length of the simulation box in the  $x$  direction,  $L$ . The bending constant was fixed to  $k_b = 0$ , and the number of liquid particles in the droplet was set to ( $n_d \simeq 4200$ ). In Figure 11, the velocity of the droplet is plotted against channel length  $L$ . Despite maintaining the number of particles in the droplet constant ( $n_d \simeq 4200$ ), and applying the same total

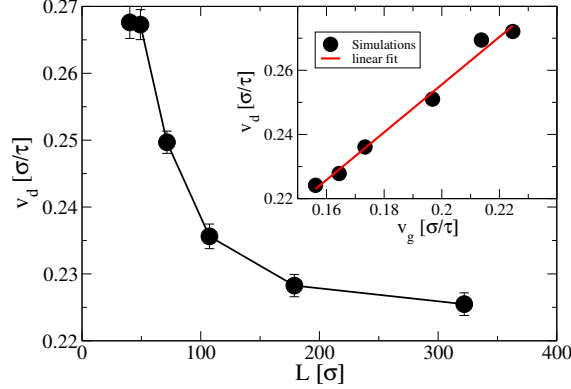


Figure 11: Droplet velocity ( $v_d$ ) as a function of the channel length ( $L$ ). Extending the channel length  $L$  is equivalent to increasing the distance between consecutive droplets, due to the periodic boundary conditions applied in the simulations. This graphic shows that the closer the droplets are to each other, the faster they move through the channel. Inset: Droplet velocity (black circles) plotted against surrounding gas velocity. Each point corresponds to a different channel length. The red continuous line is the linear regression of the data.

external body force on them, the droplet velocity varies significantly ( $\sim 16\%$ ) with  $L$ .

To verify the model of drag friction between gas and liquid ( $f_g = -\gamma_{\text{gas}}(v_d - v_{\text{gas}})$ ), the equation of motion of the droplet can be examined. The dissipative forces are proportional to the droplet velocity<sup>20,22,53</sup>  $f_{\text{dis}} = -\alpha\eta v_d$ , where  $\eta$  is the liquid viscosity, and  $\alpha$  is a constant of the order of unity. The total driving force is the sum of the body forces applied to each particle in the droplet  $F_{\text{ext}} = n_{\text{drop}}f_{\text{ext}}$ . The sum of all forces acting on the droplet must be zero on average, because the trajectory of the droplet describes a uniform linear motion:

$$0 = n_{\text{drop}}f_{\text{ext}} - \gamma_{\text{gas}}(v_d - v_{\text{gas}}) - \alpha\eta v_d \quad (15)$$

Solving for the droplet velocity yields:

$$v_d = v_{\text{gas}}\gamma_{\text{gas}}/(\gamma_{\text{gas}} + \eta\alpha) + n_{\text{drop}}f_{\text{ext}}/(\gamma_{\text{gas}} + \eta\alpha) \quad (16)$$

By plotting the velocity of the droplet ( $v_d$ ) versus the surrounding gas velocity ( $v_g$ ), we validate the drag model (see Inset of Figure 11).  $v_d$  varies linearly with  $v_g$ , as given by Eq. 16. Following Eq. 16, the friction coefficients can be estimated. We note that the influence

of the gas on the droplet velocity depends on the relative coexistence densities of the vapor ( $\rho_v$ ) and liquid ( $\rho_l$ ) phases at the given temperature. In this case the temperature was fixed at  $T = 0.8\varepsilon/k_B$ , and the coexisting densities ratio  $\rho_l/\rho_v = 0.7\sigma^{-3}/0.03\sigma^{-3} \simeq 23$ . We remark that the gas-liquid friction can have an important influence in two phase flows, and should be taken into account in rheological analysis in nano-channels.

## 4 Concluding Remarks

We studied a liquid droplet coexisting with its vapor, flowing through a nano-channel, whose walls are coated with hydrophobic semiflexible polymer brushes. It is important to note that the droplet does not wet the brush, being in a Cassie–Baxter state.

We studied the influence of the bending rigidity of the polymers on the flow, maintaining the droplet shape and mass constant. We explored a wide range of bending stiffness, which expressed as the ratio of persistence  $l_p$  over contour lengths  $l_c$  of the polymer chains, belong to the range:  $0.1 < l_p/l_c < 20$ . We found that the center of mass velocity of the droplet decreases with increasing bending constant. In particular, for the range  $l_p/l_c < 3$  the velocity of the droplet decays faster with increasing bending rigidity, than for stiffer polymers in the range  $l_p/l_c > 3$ . In order to have a better understanding of these results, we investigated the velocity field of the free terminal bead of the polymers. For flexible polymers ( $l_p/l_c < 3$ ) this velocity field shows that the monomers near the liquid move in the same direction as the droplet, while the terminal beads that are nearer to the substrate move in a direction opposite to the flow. This collective "treadmill-belt" dynamics of the chains gives rise to a positive velocity field of the brush in contact with the liquid, that allows for a faster droplet transport through the channel. For  $l_p/l_c > 3$  the space explored by terminal beads of the grafted chains is reduced, due to the bending rigidity and no cyclic motion is observed, thus reducing the droplet's velocity. The liquid boundary layer velocity relative to the brush boundary layer shows a significant increment around  $l_p/l_c \simeq 4$ . We attribute this to the

decrease in the number of liquid-polymer interactions, but further investigations should be carried out to unravel this completely.

We analyzed in addition, the deformation of the polymer brush as a function of rigidity. The elongation of the chains in the flow direction presents a maximum for polymers whose persistence length is equal to the contour length ( $l_p/l_c \simeq 1$ ). For this value of bending rigidity, the maximum compression relative to the unperturbed brush is observed. The height of the polymers as a function of persistence length was also examined, showing a good agreement with mean field theories<sup>72,74</sup> for  $l_p/l_c \leq 4$ .

For the droplet flowing in coexistence with its gas, we observe that the velocity of the gas phase decays exponentially as the distance from the droplet increases. The length of the simulations box was changed to modify the distance between consecutive droplets, therefore varying the velocity at which the droplet encounters the gas. The droplet-vapor friction force was found to depend linearly on the velocity difference between droplet and its surrounding gas, as expected in a proposed drag model. Reducing the distance between consecutive droplets increases the velocity of the flow.

Increasing the understanding of droplet flow through brush-covered surfaces offers a great opportunity to control droplet flow by taking advantage of the enormous versatility of polymer brushes as surface-modifiers. This is of great importance for microfluidics and other technological applications. Hopefully the simulation results presented in this work can be compared with upcoming experiments.

## Acknowledgement

Financial support through grants PIP 11220150100417 and PIP 11220110100646 (CONICET), BAPIN 2014, BAPIN 2017 (CNEA), PME 2015, PICT-E 134-2014 (MINCYT) is gratefully acknowledged. We thank also Marcus Müller and Ignacio Urrutia for fruitful discussions about different aspects of the present work.

## References

- (1) Weinbaum, S.; Tarbell, J. M.; Damiano, E. R. The Structure and Function of the Endothelial Glycocalyx Layer. *Annual Review of Biomedical Engineering* **2007**, *9*, 121–167, PMID: 17373886.
- (2) Lanotte, L.; Tomaiuolo, G.; Misbah, C.; Bureau, L.; Guido, S. Red blood cell dynamics in polymer brush-coated microcapillaries: A model of endothelial glycocalyx in vitro. *Biomicrofluidics* **2014**, *8*, 014104.
- (3) Cruz-Chu, E. R.; Malafeev, A.; Pajarskas, T.; Pivkin, I. V.; Koumoutsakos, P. Structure and Response to Flow of the Glycocalyx Layer. *Biophysical Journal* **2014**, *106*, 232 – 243.
- (4) Sackmann, E. K.; Fulton, A. L.; Beebe, D. J. The present and future role of microfluidics in biomedical research. *Nature* **2014**, *507*, 181 – 189.
- (5) Juang, Y.-J.; Chang, J.-S. Applications of microfluidics in microalgae biotechnology: A review. *Biotechnology Journal* **2016**, *11*, 327–335.
- (6) Volpatti, L. R.; Yetisen, A. K. Commercialization of microfluidic devices. *Trends in Biotechnology* **2014**, *32*, 347 – 350.
- (7) Song, H. Reactions in Droplets in Microfluidic Channels. *Angewandte Chemie (International ed. in English)* **2006**, *45*, 7336–7356.
- (8) Lauga, E.; Brenner, M.; Stone, H. In *Springer Handbook of Experimental Fluid Mechanics*; Tropea, C., Yarin, A. L., Foss, J. F., Eds.; Springer Berlin Heidelberg: Berlin, Heidelberg, 2007; pp 1219–1240.
- (9) Yen, T.-H.; Soong, C.-Y. Effective boundary slip and wetting characteristics of water on substrates with effects of surface morphology. *Molecular Physics* **2016**, *114*, 797–809.

- (10) Cao, B.-Y.; Chen, M.; Guo, Z.-Y. Liquid flow in surface-nanostructured channels studied by molecular dynamics simulation. *Phys. Rev. E* **2006**, *74*, 066311.
- (11) Zhang, Y. Effect of wall surface roughness on mass transfer in a nano channel. *International Journal of Heat and Mass Transfer* **2016**, *100*, 295 – 302.
- (12) Yen, T.-H. Molecular dynamics simulation of fluid containing gas in hydrophilic rough wall nanochannels. *Microfluidics and Nanofluidics* **2014**, *17*, 325–339.
- (13) Choi, C.-H.; Kim, C.-J. Large Slip of Aqueous Liquid Flow over a Nanoengineered Superhydrophobic Surface. *Phys. Rev. Lett.* **2006**, *96*, 066001.
- (14) Bixler, G. D.; Bhushan, B. Bioinspired rice leaf and butterfly wing surface structures combining shark skin and lotus effects. *Soft Matter* **2012**, *8*, 11271–11284.
- (15) Zhang, Y.-L.; Xia, H.; Kim, E.; Sun, H.-B. Recent developments in superhydrophobic surfaces with unique structural and functional properties. *Soft Matter* **2012**, *8*, 11217–11231.
- (16) Kunert, C.; Harting, J. Roughness Induced Boundary Slip in Microchannel Flows. *Phys. Rev. Lett.* **2007**, *99*, 176001.
- (17) Liakopoulos, A.; Sofos, F.; Karakasidis, T. E. Friction factor in nanochannel flows. *Microfluidics and Nanofluidics* **2016**, *20*, 1–7.
- (18) Trethewey, D. C.; Meinhart, C. D. A generating mechanism for apparent fluid slip in hydrophobic microchannels. *Physics of Fluids (1994-present)* **2004**, *16*, 1509–1515.
- (19) Lichter, S.; Martini, A.; Snurr, R. Q.; Wang, Q. Liquid Slip in Nanoscale Channels as a Rate Process. *Phys. Rev. Lett.* **2007**, *98*, 226001.
- (20) Fukushima, A.; Mima, T.; Kinefuchi, I.; Tokumasu, T. Molecular Dynamics Simulation of Channel Size Dependence of the Friction Coefficient between a Water Droplet and a Nanochannel Wall. *The Journal of Physical Chemistry C* **2015**, *119*, 28396–28404.

- (21) He, Q.; Hasegawa, Y.; Kasagi, N. Heat transfer modelling of gas liquid slug flow without phase change in a micro tube. *International Journal of Heat and Fluid Flow* **2010**, *31*, 126 – 136.
- (22) Wu, C.; Xu, X.; Qian, T. Molecular dynamics simulations for the motion of evaporative droplets driven by thermal gradients along nanochannels. *Journal of Physics: Condensed Matter* **2013**, *25*, 195103.
- (23) Günther, A.; Jhunjhunwala, M.; Thalmann, M.; Schmidt, M. A.; Jensen, K. F. Micromixing of Miscible Liquids in Segmented Gas Liquid Flow. *Langmuir* **2005**, *21*, 1547–1555, PMID: 15697306.
- (24) Chen, H.; Li, J.; Zhou, W.; Pelan, E. G.; Stoyanov, S. D.; Arnaudov, L. N.; Stone, H. A. Sonication Microfluidics for Fabrication of Nanoparticle-Stabilized Microbubbles. *Langmuir* **2014**, *30*, 4262–4266, PMID: 24694278.
- (25) Kelly, S.; Balhoff, M. T.; Torres-Verdín, C. Quantification of Bulk Solution Limits for Liquid and Interfacial Transport in Nanoconfinements. *Langmuir* **2015**, *31*, 2167–2179, PMID: 25630047.
- (26) Kuhn, S.; Hartman, R. L.; Sultana, M.; Nagy, K. D.; Marre, S.; Jensen, K. F. Teflon-Coated Silicon Microreactors: Impact on Segmented Liquid-Liquid Multiphase Flows. *Langmuir* **2011**, *27*, 6519–6527, PMID: 21510687.
- (27) Mawatari, K.; Kubota, S.; Xu, Y.; Priest, C.; Sedev, R.; Ralston, J.; Kitamori, T. Femtoliter Droplet Handling in Nanofluidic Channels: A Laplace Nanovalve. *Analytical Chemistry* **2012**, *84*, 10812–10816, PMID: 23214507.
- (28) Shui, L.; Eijkel, J. C.; van den Berg, A. Multiphase flow in microfluidic systems Control and applications of droplets and interfaces. *Advances in Colloid and Interface Science* **2007**, *133*, 35 – 49.

- (29) Rebrov, E. V. Two-phase flow regimes in microchannels. *Theoretical Foundations of Chemical Engineering* **2010**, *44*, 355–367.
- (30) Zhang, F. Y.; Yang, X. G.; Wang, C. Y. Liquid Water Removal from a Polymer Electrolyte Fuel Cell. *Journal of The Electrochemical Society* **2006**, *153*, A225–A232.
- (31) Lu, Z.; Kandlikar, S.; Rath, C.; Grimm, M.; Domigan, W.; White, A.; Hardbarger, M.; Owejan, J.; Trabold, T. Water management studies in {PEM} fuel cells, Part II: Ex situ investigation of flow maldistribution, pressure drop and two-phase flow pattern in gas channels. *International Journal of Hydrogen Energy* **2009**, *34*, 3445 – 3456.
- (32) Cheah, M. J.; Kevrekidis, I. G.; Benziger, J. B. Water Slug to Drop and Film Transitions in Gas-Flow Channels. *Langmuir* **2013**, *29*, 15122–15136, PMID: 24206393.
- (33) Seemann, R.; Brinkmann, M.; Pfohl, T.; Herminghaus, S. Droplet based microfluidics. *Rep. Prog. Phys.* **2012**, *75*, 016601.
- (34) Wei, Q.; Cai, M.; Zhou, F.; Liu, W. Dramatically Tuning Friction Using Responsive Polyelectrolyte Brushes. *Macromolecules* **2013**, *46*, 9368–9379.
- (35) Chen, T.; Ferris, R.; Zhang, J.; Ducker, R.; Zauscher, S. Stimulus-responsive polymer brushes on surfaces: Transduction mechanisms and applications. *Progress in Polymer Science* **2010**, *35*, 94 – 112, Special Issue on Stimuli-Responsive Materials.
- (36) Chen, W.-L.; Cordero, R.; Tran, H.; Ober, C. K. 50th Anniversary Perspective: Polymer Brushes: Novel Surfaces for Future Materials. *Macromolecules* **2017**, *0*, null.
- (37) Ma, S.; Wang, D.; Liang, Y.; Sun, B.; Gorb, S. N.; Zhou, F. Gecko-Inspired but Chemically Switched Friction and Adhesion on Nanofibrillar Surfaces. *Small* **2015**, *11*, 1131–1137.
- (38) Azzaroni, O. Polymer brushes here, there, and everywhere: Recent advances in their

- practical applications and emerging opportunities in multiple research fields. *Journal of Polymer Science Part A: Polymer Chemistry* **2012**, *50*, 3225–3258.
- (39) Das, S.; Banik, M.; Chen, G.; Sinha, S.; Mukherjee, R. Polyelectrolyte brushes: theory, modelling, synthesis and applications. *Soft Matter* **2015**, *11*, 8550–8583.
- (40) Yameen, B.; Ali, M.; Neumann, R.; Ensinger, W.; Knoll, W.; Azzaroni, O. Single Conical Nanopores Displaying pH-Tunable Rectifying Characteristics. Manipulating Ionic Transport With Zwitterionic Polymer Brushes. *Journal of the American Chemical Society* **2009**, *131*, 2070–2071, PMID: 19159287.
- (41) Costantini, F.; Bula, W. P.; Salvio, R.; Huskens, J.; Gardeniers, H. J. G. E.; Reinhoudt, D. N.; Verboom, W. Nanostructure Based on Polymer Brushes for Efficient Heterogeneous Catalysis in Microreactors. *Journal of the American Chemical Society* **2009**, *131*, 1650–1651, PMID: 19143524.
- (42) Yu, Q.; Zhang, Y.; Chen, H.; Zhou, F.; Wu, Z.; Huang, H.; Brash, J. L. Protein Adsorption and Cell Adhesion/Detachment Behavior on Dual-Responsive Silicon Surfaces Modified with Poly(N-isopropylacrylamide)-block-polystyrene Copolymer. *Langmuir* **2010**, *26*, 8582–8588, PMID: 20170172.
- (43) Pastorino, C.; Binder, K.; Müller, M. Coarse-Grained Description of a Brush-Melt Interface in Equilibrium and under Flow. *Macromolecules* **2009**, *42*, 401–410.
- (44) Lee, T.; Hendy, S. C.; Neto, C. Interfacial Flow of Simple Liquids on Polymer Brushes: Effect of Solvent Quality and Grafting Density. *Macromolecules* **2012**, *45*, 6241–6252.
- (45) Sokoloff, J. B. Theory of Friction between Neutral Polymer Brushes. *Macromolecules* **2007**, *40*, 4053–4058.
- (46) Desai, P. R.; Sinha, S.; Das, S. Compression of polymer brushes in the weak interpen-

- tration regime: scaling theory and molecular dynamics simulations. *Soft Matter* **2017**,  
–.
- (47) Zhu, Y.; ; Granick, S. Apparent Slip of Newtonian Fluids Past Adsorbed Polymer Layers. *Macromolecules* **2002**, *35*, 4658–4663.
- (48) Klein, J.; Kumacheva, E.; Mahalu, D.; Perahia, D.; Fetters, L. J. Reduction of frictional forces between solid surfaces bearing polymer brushes. *Nature* **1994**, *636*.
- (49) Zhang, R.; Ma, S.; Wei, Q.; Ye, Q.; Yu, B.; van der Gucht, J.; Zhou, F. The Weak Interaction of Surfactants with Polymer Brushes and Its Impact on Lubricating Behavior. *Macromolecules* **2015**, *48*, 6186–6196.
- (50) Charrault, E.; Lee, T.; Easton, C. D.; Neto, C. Boundary flow on end-grafted PEG brushes. *Soft Matter* **2016**, *12*, 1906–1914.
- (51) Chennevière, A.; Cousin, F.; Boué, F.; Drockenmuller, E.; Shull, K. R.; Léger, L.; Restagno, F. Direct Molecular Evidence of the Origin of Slip of Polymer Melts on Grafted Brushes. *Macromolecules* **2016**, *49*, 2348–2353.
- (52) Deng, M.; Li, X.; Liang, H.; Caswell, B.; Karniadakis, G. E. Simulation and modelling of slip flow over surfaces grafted with polymer brushes and glycocalyx fibres. *Journal of Fluid Mechanics* **2012**, *711*, 192–211.
- (53) Leonforte, F.; Servantie, J.; Pastorino, C.; Müller, M. Molecular transport and flow past hard and soft surfaces: computer simulation of model systems. *Journal of Physics: Condensed Matter* **2011**, *23*, 184105.
- (54) Priezjev, N. V. Shear rate threshold for the boundary slip in dense polymer films. *Phys. Rev. E* **2009**, *80*, 031608.
- (55) Priezjev, N. V.; Troian, S. M. Molecular Origin and Dynamic Behavior of Slip in Sheared Polymer Films. *Phys. Rev. Lett.* **2004**, *92*, 018302.

- (56) Müller, M.; Pastorino, C.; Servantie, J. Flow, slippage and a hydrodynamic boundary condition of polymers at surfaces. *Journal of Physics: Condensed Matter* **2008**, *20*, 494225.
- (57) Müller, M.; MacDowell, L. G. Interface and Surface Properties of Short Polymers in Solution: Monte Carlo Simulations and Self-Consistent Field Theory. *Macromolecules* **2000**, *33*, 3902–3923.
- (58) Kreer, T. Polymer-brush lubrication: a review of recent theoretical advances. *Soft Matter* **2016**, *12*, 3479–3501.
- (59) Kim, Y. W.; Lobaskin, V.; Gutsche, C.; Kremer, F.; Pincus, P.; Netz, R. R. Nonlinear Response of Grafted Semiflexible Polymers in Shear Flow. *Macromolecules* **2009**, *42*, 3650–3655.
- (60) Römer, F.; Fedosov, D. A. Dense brushes of stiff polymers or filaments in fluid flow. *EPL (Europhysics Letters)* **2015**, *109*, 68001.
- (61) Singh, M. K.; Ilg, P.; Espinosa-Marzal, R. M.; Spencer, N. D.; Kröger, M. Influence of Chain Stiffness, Grafting Density and Normal Load on the Tribological and Structural Behavior of Polymer Brushes: A Nonequilibrium-Molecular-Dynamics Study. *Polymers* **2016**, *8*.
- (62) Speyer, K.; Pastorino, C. Brushes of semiflexible polymers in equilibrium and under flow in a super-hydrophobic regime. *Soft Matter* **2015**, *11*, 5473–5484.
- (63) Nikoubashman, A.; Milchev, A.; Binder, K. Dynamics of single semiflexible polymers in dilute solution. *The Journal of Chemical Physics* **2016**, *145*, 234903.
- (64) Hoogerbrugge, P. J.; Koelman, J. M. V. A. Simulating microscopic hydrodynamic phenomena with dissipative particle dynamics. *EPL (Europhysics Letters)* **1992**, *19*, 155.

- (65) Español, P. Hydrodynamics from dissipative particle dynamics. *Phys. Rev. E* **1995**, *52*, 1734–1742.
- (66) Soddemann, T.; Dünweg, B.; Kremer, K. Dissipative particle dynamics: A useful thermostat for equilibrium and nonequilibrium molecular dynamics simulations. *Phys. Rev. E* **2003**, *68*, 046702.
- (67) Pastorino, C.; Kreer, T.; Müller, M.; Binder, K. Comparison of dissipative particle dynamics and Langevin thermostats for out-of-equilibrium simulations of polymeric systems. *Phys. Rev. E* **2007**, *76*, 026706.
- (68) Pastorino, C.; Binder, K.; Kreer, T.; Müller, M. Static and dynamic properties of the interface between a polymer brush and a melt of identical chains. *The Journal of Chemical Physics* **2006**, *124*, 064902.
- (69) Müller, M.; Pastorino, C. Cyclic motion and inversion of surface flow direction in a dense polymer brush under shear. *EPL (Europhysics Letters)* **2008**, *81*, 28002.
- (70) Pastorino, C.; Müller, M. Mixed brush of chemically and physically adsorbed polymers under shear: Inverse transport of the physisorbed species. *The Journal of Chemical Physics* **2014**, *140*, –.
- (71) Ramakrishna, S. N.; Cirelli, M.; Divandari, M.; Benetti, E. M. Effects of Lateral Deformation by Thermoresponsive Polymer Brushes on the Measured Friction Forces. *Langmuir* **2017**, *33*, 4164–4171, PMID: 28394137.
- (72) Birshtein, T.; Zhulina, Y. Conformations of polymer chains grafted to an impermeable plane surface. *Polymer Science U.S.S.R.* **1983**, *25*, 2165 – 2174.
- (73) Milchev, A.; Binder, K. Unconventional ordering behavior of semi-flexible polymers in dense brushes under compression. *Soft Matter* **2014**, *10*, 3783–3797.

- (74) Egorov, S. A.; Hsu, H.-P.; Milchev, A.; Binder, K. Semiflexible polymer brushes and the brush-mushroom crossover. *Soft Matter* **2015**, –.

# Graphical TOC Entry

